

Molecular Physics

An International Journal at the Interface Between Chemistry and Physics

ISSN: 0026-8976 (Print) 1362-3028 (Online) Journal homepage: <http://www.tandfonline.com/loi/tmph20>

Phase diagram of the ST2 model of water

Frank Smallenburg, Peter H. Poole & Francesco Sciortino

To cite this article: Frank Smallenburg, Peter H. Poole & Francesco Sciortino (2015) Phase diagram of the ST2 model of water, *Molecular Physics*, 113:17-18, 2791-2798, DOI: 10.1080/00268976.2015.1043966

To link to this article: <http://dx.doi.org/10.1080/00268976.2015.1043966>



Published online: 18 May 2015.



Submit your article to this journal [↗](#)



Article views: 100



View related articles [↗](#)



View Crossmark data [↗](#)



Citing articles: 2 View citing articles [↗](#)

INVITED ARTICLE

Phase diagram of the ST2 model of water

Frank Smallenburg^{a,*}, Peter H. Poole^b and Francesco Sciortino^c^a*Institut für Theoretische Physik II: Weiche Materie, Heinrich-Heine Universität Düsseldorf, Düsseldorf, Germany;* ^b*Department of Physics, St. Francis Xavier University, Nova Scotia, Canada;* ^c*Dipartimento di Fisica, Università di Roma La Sapienza, Roma, Italy*

(Received 19 February 2015; accepted 2 April 2015)

We evaluate the free energy of the fluid and crystal phases for the ST2 potential with reaction field corrections for the long-range interactions. We estimate the phase coexistence boundaries in the temperature–pressure plane, as well as the gas–liquid critical point and gas–liquid coexistence conditions. Our study frames the location of the previously identified liquid–liquid critical point relative to the crystalline phase boundaries, and opens the way for exploring crystal nucleation in a model where the metastable liquid–liquid critical point is computationally accessible.

Keywords: water models; phase diagrams; computer simulations; free energies

1. Introduction

The thermodynamic behaviour of water at low temperatures is unconventional. Several quantities, e.g. the isobaric density ρ , the isothermal compressibility K_T , and the constant-pressure specific heat C_P , are characterised by non-monotonic temperature or pressure dependence [1]. Over the past decades, the anomalous behaviour of these quantities has attracted the attention of numerous researchers. In 1992, a numerical investigation of the equation of state (EOS) suggested the presence of a liquid–liquid (LL) critical point [2] in the ST2 model [3], an interaction potential that describes water as a classical, rigid, and non-polarisable molecule. The presence of an LL critical point (LLCP), located in the supercooled region, provides an elegant explanation of the thermodynamic anomalies that characterise liquid water and which become more pronounced close to such a critical point [4].

The conceptual novelty of a one-component system with more than one liquid phase has stimulated the scientific community to deeply probe the physical origin of this phenomenon [5–13]. It is now clear that an LLCP, while common in tetrahedral network-forming liquids [14–19], can also be observed in complex one-component fluids when the (spherically symmetric) interaction potential generates two competing length scales [20–23]. In the last few years, the interest has shifted towards the interplay between the LL critical point and the crystal nucleation [18,24–27]. Indeed, in experiments, crystallisation has so far prevented direct observation of this phenomenon in a one-component bulk system. Only recently have computer simulations demonstrated the possibility of generating a thermodynamically

stable LL critical point (as opposed to a metastable one) in models of network-forming liquids [18,19].

Accurate information on the phase coexistence boundaries between disordered and ordered phases is relevant not only to establish the thermodynamic fields of stability of the different phases, but also as a reference for estimating when the liquid becomes metastable. In turn, this has relevance for estimating when the barrier to crystallisation becomes finite and how rapidly the barrier decreases on supercooling [28]. Except for one early report focussing on the liquid–ice I_h boundary [29], none of the coexistence lines between the gas, liquid, and the many phases of crystalline ice have been accurately determined for the ST2 model. In this article, we fill this gap and evaluate these coexistence boundaries by calculating the fluid chemical potential (via thermodynamic integration) and the crystal chemical potential (via the Frenkel–Ladd method [30], extended to molecules [31]). We test several crystals (ice I_h , I_c , II, III, VI, VII, and VIII) and find that in the region of pressure where thermodynamic anomalies appear (e.g. near the lines of maxima of C_P and K_T) ice I_h and I_c have the same free energy within our numerical precision. Unexpectedly, we discover that for the ST2 model, on increasing pressure, the stable phase is a dense tetragonal crystal with a partial proton order. This structure has a free energy about $0.4 k_B T$ lower than ice VII, the structure obtained by interspersing two I_c lattices (here, T is the temperature and k_B is the Boltzmann constant). We also evaluate the (metastable) line of coexistence for the recently reported ice 0 lattice [32,33], a structure which could act (according to the Ostwald rule) as the intermediate phase in the process

*Corresponding author. Email: f.smallenburg@gmail.com; Frank.Smallenburg@uni-duesseldorf.de

of nucleating the stable ice $I_{h/c}$ crystal from the fluid. For completeness, we determine the location of the gas–liquid critical point, which is found to be at $T_c = 558.0 \pm 0.3\text{K}$ and $\rho_c = 0.265 \pm 0.005 \text{g/cm}^3$.

2. Model and simulation methods

We study, via Monte Carlo (MC) simulations, the original ST2 potential as defined by Rahman and Stillinger [3], with reaction field corrections to approximate the long-range contributions to the electrostatic interactions. ST2 models water as a rigid body with an oxygen atom at the centre and four charges $q = \pm 0.4e$ (where e is the electron charge), two positive and two negative, in a tetrahedral geometry. The distances from the oxygen to the positive and negative charges are 0.1 and 0.08 nm, respectively. The oxygen–oxygen interaction is modelled via a standard Lennard-Jones potential truncated at $2.5\sigma_{\text{LJ}}$, with $\sigma_{\text{LJ}} = 0.31 \text{ nm}$ and $\epsilon_{\text{LJ}} = 0.31694 \text{ kJ/mol}$. The Lennard-Jones residual interactions are handled through standard long-range corrections, i.e. by assuming that the radial distribution function is unity beyond the cutoff. The charge–charge interactions are smoothly switched off both at small and large distances via a tapering function, as in the original model [3]. Complete details of the simulation procedure are as described in Ref. [2]. In the following, we use $\sigma = 1 \text{ nm}$ as the unit of length.

2.1. Thermodynamic integration: fluid free energy

To evaluate the fluid free energy, we perform a thermodynamic integration along a path of constant reference density ρ_{ref} for a modified pair potential,

$$V = \min(V_{\text{ST2}}, 200 \text{ kJ/mol}). \quad (1)$$

This potential coincides with the ST2 potential for all intermolecular distances and orientations where $V_{\text{ST2}} < 200 \text{ kJ/mol}$, and is constant and equal to 200 kJ/mol otherwise. Note that in the temperature range where we investigate the phase behaviour, molecules never approach close enough to reach this limit. In this way, the divergence of the potential energy for configurations in which some intermolecular separations vanish (which would otherwise be probed at very high temperatures) is eliminated and the infinite temperature limit is properly approximated by an ideal gas of molecules at the same density.

The fluid free energy (per particle) is calculated as

$$\beta f_{\text{ST2}}^{\text{fluid}}(\beta, \rho_{\text{ref}}) = \beta f_{\text{ig}}(\beta, \rho_{\text{ref}}) + \int_0^\beta \langle V(\beta, \rho_{\text{ref}}) \rangle d\beta, \quad (2)$$

where $\beta = 1/k_{\text{B}}T$ and $\beta f_{\text{ig}}(\beta, \rho) = \log(\rho_n \sigma^3) - 1$ is the ideal gas free energy and ρ_n is the number density. Figure 1 shows

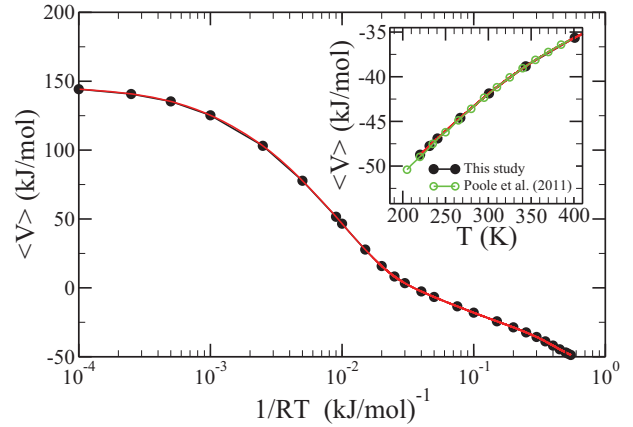


Figure 1. Average pair potential energy $\langle V \rangle$ vs. $(RT)^{-1}$ at $\rho = 1.0 \text{ g/cm}^3$ (with R the ideal gas constant). Symbols are MC data, and the line is the spline function used in the numerical integration. The inset shows the same data as a function of T and compares them to previously published data for the ST2 potential [34].

the average modified pair potential energy $\langle V(\beta, \rho) \rangle$ and the interpolating (spline) continuous curve used to numerically evaluate the integral. The free energy at different densities along a constant- T path is evaluated via thermodynamic integration of the EOS.

$$\beta f_{\text{ST2}}^{\text{fluid}}(T, \rho_n) = \beta f_{\text{ST2}}^{\text{fluid}}(T, \rho_{n,\text{ref}}) + \int_{\rho_{n,\text{ref}}}^{\rho_n} \frac{\beta P(\rho'_n)}{\rho'_n} d \ln(\rho'_n), \quad (3)$$

where $P(\rho_n)$ is the EOS for the pressure P at fixed T .

2.2. Crystal free energy

To evaluate the free energy of a selected crystalline structure, we follow the methodology reviewed in Ref. [31]. We define an Einstein crystal in which each molecule interacts, in addition to the ST2 potential, with a Hamiltonian, composed of a translational (H_{trans}) and a rotational (H_{rot}) part, that attaches each molecule to a reference position and orientation. For each particle, we define two unit vectors: the (normalised) HH vector and the dipole vector, named respectively \vec{a} and \vec{b} . The reference configuration is defined by the reference position of the oxygen atom \mathbf{r}_0 and the reference position of \vec{a} and \vec{b} [31,35]. In the following, we indicate with $\mathbf{r} - \mathbf{r}_0$ the displacement of a particle located at \mathbf{r} from its reference position, and with ϕ_a and ϕ_b the angles between \vec{a} and \vec{b} and their reference values. More precisely,

$$H_{\text{Einstein}} = H_{\text{trans}} + H_{\text{rot}}, \quad (4)$$

with

$$H_{\text{trans}} = \lambda_t (\mathbf{r} - \mathbf{r}_0)^2 / \sigma^2 \quad (5)$$

Table 1. Free energy βf of the fluid and crystal phases at selected points. The value for the residual entropy in βf_6 was taken from Ref. [38]. The columns marked βf_i indicate the various contributions from the crystal free energy calculation. For the fluid, we used thermodynamic integration from an ideal gas at constant density, as explained in the text. Note that the ice III crystal listed here is proton-ordered.

	T (K)	ρ (g/cm ³)	N	λ_r (kJ/mol)	λ_t (kJ/mol)	βf	βf_1	βf_2	$\beta f_3 + \beta f_4$	βf_5	βf_6
Ice I _h	270	0.8715	21952	$3 \cdot 10^4$	$3 \cdot 10^6$	-8.829	19.440	15.064	-19.640	-23.282	-0.410
Ice I _c	270	0.8715	21952	$3 \cdot 10^4$	$3 \cdot 10^6$	-8.829	19.440	15.064	-19.658	-23.264	-0.410
Ice II	230	1.16291	9216	$3 \cdot 10^4$	$3 \cdot 10^6$	-11.649	19.678	15.305	-19.821	-26.811	0
Ice III	230	1.16756	6144	$3 \cdot 10^4$	$3 \cdot 10^6$	-11.699	19.677	15.305	-20.0548	-26.626	0
Ice VI	250	1.27356	8100	$3 \cdot 10^4$	$3 \cdot 10^6$	-10.772	19.678	15.305	-20.349	-25.996	-0.410
Ice VII	270	1.5804	21296	$3 \cdot 10^4$	$3 \cdot 10^6$	-8.230	19.440	15.064	-19.318	-23.006	-0.410
Ice VII*	270	1.6250	6912	$3 \cdot 10^4$	$3 \cdot 10^6$	-8.59	19.440	15.064	-19.112	-23.567	-0.410
Ice VIII	270	1.55645	1152	$3 \cdot 10^4$	$3 \cdot 10^6$	-6.852	19.4185	15.064	-19.061	-22.274	0
Ice 0	250	0.8494	29160	$3 \cdot 10^4$	$3 \cdot 10^6$	-10.399	19.555	15.180	-19.983	-24.741	-0.410
Fluid	270	1.002	268	—	—	-8.4411	—	—	—	—	—

and

$$H_{\text{rot}} = \lambda_r \left[\sin^2 \phi_a + \left(\frac{\phi_b}{\pi} \right)^2 \right]. \quad (6)$$

Here, λ_t and λ_r indicate the strength of the coupling to the reference configuration. Again following Ref. [31], the free energy (per particle) of a crystal structure f^{xt} , in the limit of large λ_r and λ_t is calculated as

$$\beta f^{\text{xt}} = \beta f_1 + \beta f_2 + \beta f_3 + \beta f_4 + \beta f_5 + \beta f_6, \quad (7)$$

where indicating with N the number of molecules in the system,

$$\begin{aligned} \beta f_1 &= -\frac{1}{N} \ln \left[\left(\frac{\pi}{\beta \lambda_t} \right)^{\frac{3(N-1)}{2}} N^{\frac{3}{2}} \frac{1}{\rho_n \sigma^3} \right] \\ \beta f_2 &= -\ln \frac{\sqrt{\pi}}{4} + 1.5 \ln(\beta \lambda_r) \\ \beta f_3 &= \int_0^{\lambda_t} \langle \beta H_{\text{trans}} \rangle_\lambda d \ln \lambda \\ \beta f_4 &= \int_0^{\lambda_r} \langle \beta H_{\text{rot}} \rangle_\lambda d \ln \lambda \\ \beta f_5 &= -\frac{\ln \langle e^{-\beta V_{\text{ST2}}} \rangle_{\lambda_r, \lambda_t}}{N} \\ \beta f_6 &= \begin{cases} \ln[1.5] & \text{(full proton-disordered crystal)} \\ 0 & \text{(proton-ordered crystal).} \end{cases} \quad (8) \end{aligned}$$

The symbols $\langle H_{\text{rot}} \rangle_\lambda$ and $\langle H_{\text{trans}} \rangle_\lambda$ indicate the average values of H_{rot} and H_{trans} calculated from an MC simulation of particles interacting via the ST2 potential complemented by H_{Einstein} . The symbol $\langle e^{-\beta V_{\text{ST2}}} \rangle_{\lambda_r, \lambda_t}$ indicates the average value of $e^{-\beta V_{\text{ST2}}}$ (where V_{ST2} is the system ST2 potential energy) in a simulation in which the particles interact with each other via the ST2 potential and with the Einstein

Hamiltonian with values λ_r and λ_t . In all simulations carried out to perform the integration, the centre of mass of the system is kept fixed [36].

Finally, βf_6 indicates the contribution of proton disorder, evaluated according to Pauling's estimate [37]. More recent calculations have essentially confirmed Pauling's value [38].

Table 1 reports the values of βf_i for a few representative cases.

2.3. Grand canonical simulation: gas–liquid phase coexistence

To evaluate the gas–liquid coexistence and the location of the gas–liquid critical point, we perform grand-canonical MC simulations to evaluate at fixed T , volume v , and chemical potential μ , the probability p of observing N particles in the simulated volume. To overcome the large free-energy barriers separating the gas and liquid phases, we implement the successive umbrella sampling (SUS) technique [39]. Since this method has been applied previously to ST2 [40] to estimate the LL coexistence conditions, and has been documented in detail in these works, we refer the interested reader to the original literature.

2.4. Proton position in the crystal structures

To generate proton-disordered crystals, such as ice I_{h/c} and ice VII, one needs to assign protons to the oxygens, located at the lattice positions, so as to satisfy the ice rules. To this end, we first calculate a list of all bonded oxygen neighbours (where four bonds connect to each oxygen atom) and then decorate the oxygen lattice by assigning the proton for each bond to one of the two bonded atoms, iterating the following procedure: (1) Randomly select one oxygen with less than two hydrogens and one of the remaining undecorated bonds emanating from the selected oxygen. (2) Randomly follow the path of undecorated bonds until the path loops back to

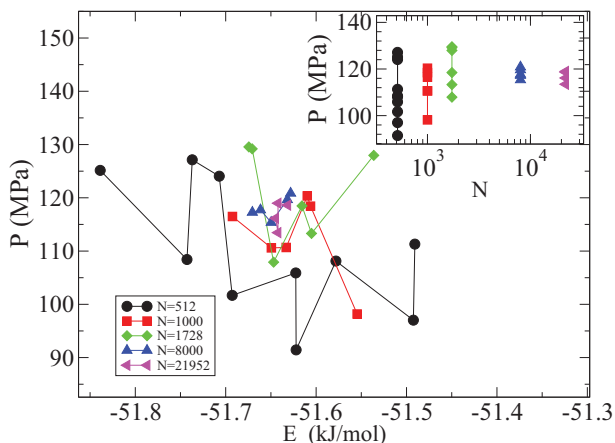


Figure 2. Size effects associated with proton disorder in configurations with zero net dipole moment: relation between the average pressure and the average energy of different proton-disordered configurations, for different number N of molecules. For all cases, the structure is ice I_c at $T = 270$ K and $\rho = 0.8715$ g/cm³. The inset shows the average pressure in different proton-disordered configurations for different number of molecules.

the original oxygen. (3) Decorate all bonds of the selected path with one proton each, associating the protons to the oxygens encountered in the path. The procedure is iterated until all oxygens have two protons associated with them. Paths in which the initial and final oxygen atoms coincide only via periodic images produce a non-zero dipole moment and should be rejected if the net dipole moment of the cell is to vanish.

To account for all possible proton realisations, one needs to investigate large systems or average over several configurations. Indeed, we find that there is a significant correlation between the proton realisation and the average potential energy E and the average pressure P (at constant volume). Figure 2 correlates P and E for each realisation, while the inset shows P in different realisations for system sizes from $N = 512$ to $N = 21,952$ molecules. Only for 8000 or more particles is the variance between different realisations within a few MPa and a 10th of a kJ/mol, the tolerance required to allow for a precise determination of the thermodynamic variables entering into the free-energy calculation. Unless otherwise stated, we have analysed configurations with 8000 or more particles for all proton-disordered crystals.

3. Results

3.1. Gas–liquid coexistence

Figure 3 shows the results of the SUS calculations. Panel (a) shows the probability p of finding N particles at fixed T and v at the coexistence chemical potential μ_c for different T . μ_c is evaluated by reweighting the histogram $p(N)$ with respect to N , such that the area below the gas and the liquid

peak is identical (0.5). At low T , the probability minimum separating the two phases is more than 50 orders of magnitude lower than the peak heights, highlighting the need for a numerical technique (like SUS) that allows the observation of rare states. Close to the critical point [panel (b)], the probability of exploring intermediate densities between the gas and the liquid becomes significant and $p(N)$ [or $p(\rho)$] assumes the characteristic shape typical of all systems belonging to the same universality class. Panel (c) compares $p(N + sE)$, where E is the potential energy of the configuration and s is the so-called mixing field parameter [41], with the theoretical expression for the magnetisation in the Ising model. To reinforce the identification of the critical point with the Ising universality class, the inset shows the finite size scaling of the critical T (defined as the T , for each size, at which the fluctuations in $N + sE$ are best fitted with the Ising form) as a function of $L^{(1 + \theta)/\nu} = L^{-2.448}$, with $\theta = 0.54$ and $\nu = 0.630$ [42,43]. The extrapolation to $L \rightarrow \infty$ suggests that the gas–liquid critical point for the reaction field ST2 model is $T_c = 558.0 \pm 0.3$ K and $\rho_c = 0.265 \pm 0.005$ g/cm³. Finally, panel (d) shows the gas–liquid coexistence in the $\rho - T$ plane. A clear nose appears around $T = 300$ K, signalling the onset of the network of hydrogen bonds (HB). Indeed, strong directional interactions (such as the HB), impose a strong coupling between density and energy. The formation of a fully bonded tetrahedral network (the expected thermodynamically stable state at low T) requires a well-defined minimum local density, which for the present model is approximately $\rho = 0.8$ g/cm³. Hence, at low T , the density of the network coexisting with the gas must approach this value. For completeness, the inset in panel (d) reports the value of $\beta\mu_c$ along the coexistence line.

3.2. Fluid–crystal coexistence

We have investigated the stability of crystal phases that may coexist with the fluid at low T . In particular, we have determined the free energies of ices I_c , I_h , II, III, VI, VII, and VIII, as well as the recently proposed metastable ice 0 structure [32]. Note that with the exception of ice VIII, all these phases have disordered hydrogen bonding. Examples of our thermodynamic integration results are reported in Figure 4, where we plot the reduced chemical potential $\beta\mu \equiv \beta f + \beta P/\rho_n$ of different phases at two selected T . For each pressure interval, the lowest chemical potential phase is the thermodynamically stable one. Intersections of different curves locate coexistence points, either stable or metastable. We then interpolate the fluid and crystal free energies based on the EOS to draw the coexistence lines in the phase diagram.

The complete phase diagram is reported in Figure 5. At low T and low P , the most stable crystal structure is the ice I lattice. From our simulations, the cubic (I_c) and hexagonal (I_h) ice structures have the same free energy within our numerical accuracy. At positive pressures, the liquid

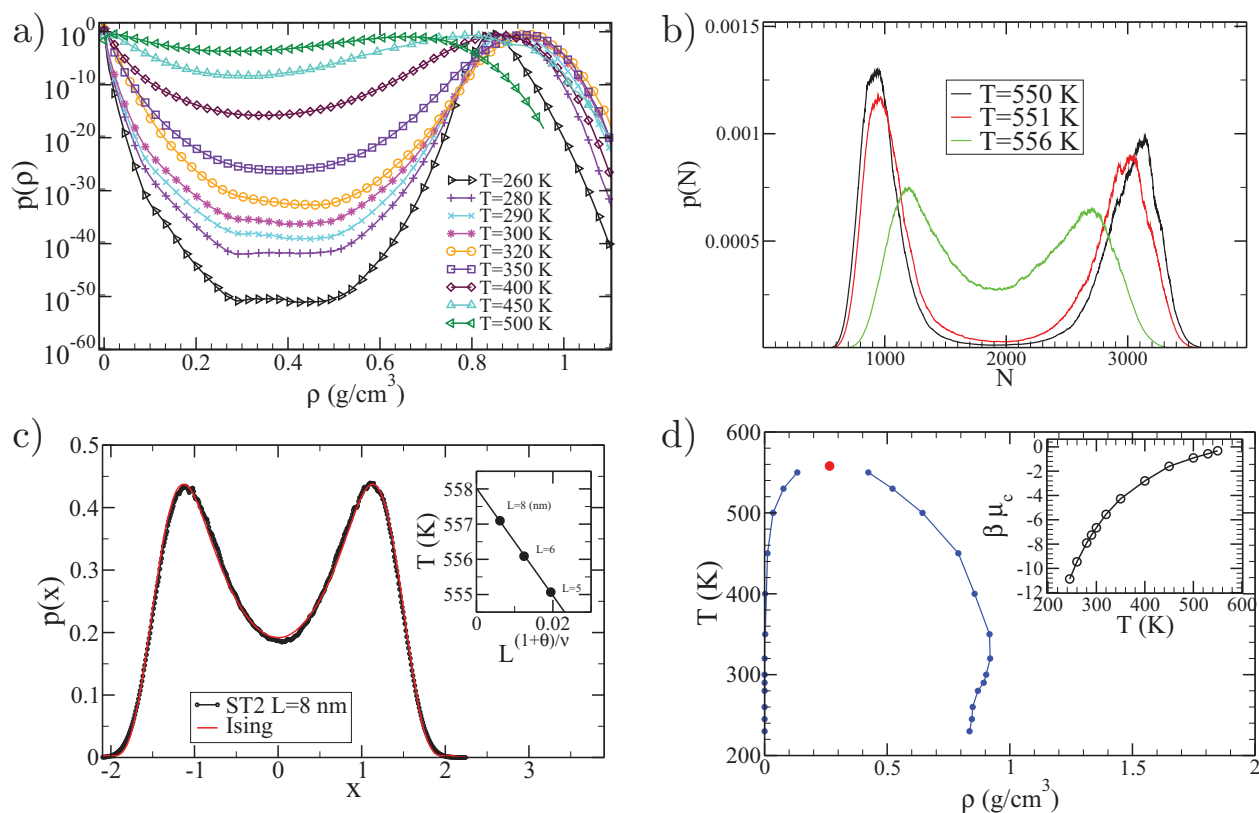


Figure 3. Gas-liquid coexistence for the ST2 model. (a) Distribution of the density fluctuations in gas-liquid coexisting states for different T for system size $L = 2$ nm. (b) Same data as in (a) but for T close to the critical temperature T_c and for $L = 6$ nm. (c) Comparison of the fluctuation in the order parameter x (a linear combination of N and E) with the theoretical expression for the three-dimension Ising model. The inset shows the finite size scaling of the critical temperature. (d) Resulting gas-liquid phase diagram in the $T - \rho$ plane. The inset shows the values of the chemical potential along the coexistence.

phase coexisting with ice I is always denser than ice, and as a result, the melting temperature of ice I decreases with increasing P . At negative P (near $P = -80$ MPa), the ice I and liquid phases coexist at the same density, and the melting temperature reaches a maximum. We note that we

have confirmed the ice $I_{h/c}$ melting temperature calculated via thermodynamic integration at two separate pressures using direct coexistence simulations, and find good agreement. We note that for the ST2-Ewald model, the melting temperature of I_c at the single pressure of 260 MPa was

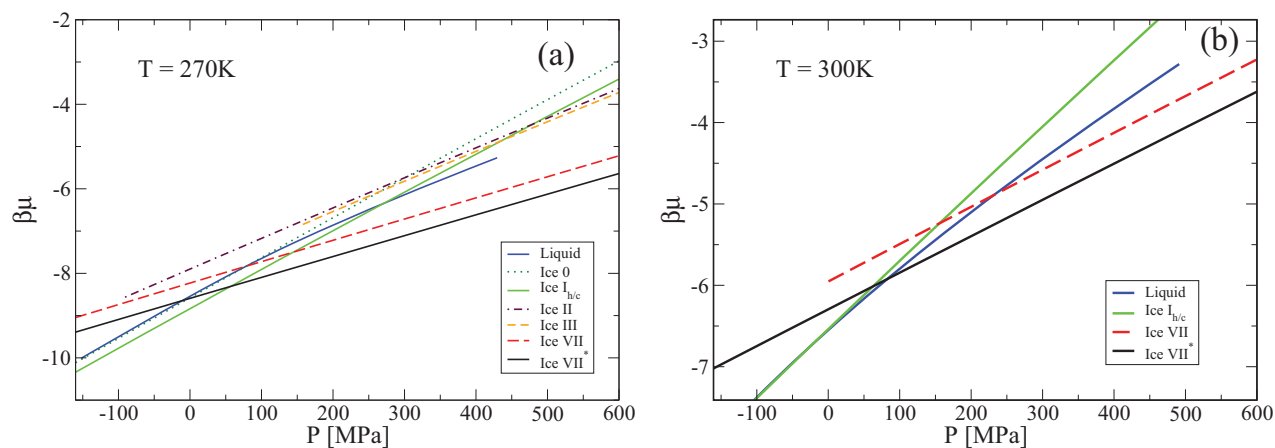


Figure 4. Reduced chemical potential $\beta\mu$ as a function of pressure P for competing phases at $T = 270$ K and $T = 300$ K. At each pressure, the phase with the lowest chemical potential is the stable one. Crossings indicate (metastable or stable) phase transitions. Note that the ice III phase in (a) is proton-ordered.

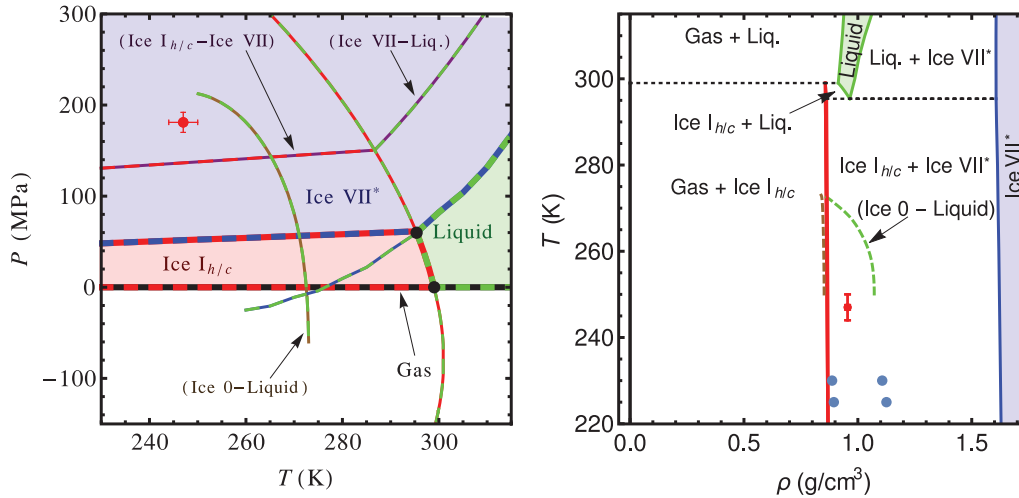


Figure 5. (a) Pressure–temperature phase diagram for the ST2 model with reaction field. In this P – T region, the stable phases are the ice VII*, cubic or hexagonal ice (ice $I_{h/c}$), gas, and liquid. The thick lines indicate phase boundaries between stable phases, while the thinner lines denote metastable phase transitions. The full circle indicates the location of the liquid–liquid critical point and its error bars, as estimated in Ref. [44]. (b) Temperature–density representation of the same phase diagram. White regions indicate two-phase coexistence. Filled regions indicate areas of one-phase stability for the different phases. Solid lines indicate coexistence densities. Note that the one-phase stability field of ice $I_{h/c}$ is centred on the optimal crystal density and is very narrow, comparable in width to the coexistence lines. Horizontal dotted lines correspond to triple points. We use the same colour-coding as in (a). The blue dots indicate the coexisting densities of the low- and high-density liquids, from Ref. [40]. The red square is the estimated location of the LL critical point.

estimated to be around 274 K, consistent with the present estimate [25].

At high pressure, the main candidate structures are the proton-ordered ice VIII structure, and the proton-disordered ice VII structure. Both structures consist of two interpenetrating I_c lattices (somewhat distorted in the case of proton-ordering), where the oxygen positions form a body-centered cubic (BCC) lattice. According to our free-energy calculations, the disordered ice VII is the more stable one in the region where coexistence with the fluid might occur. However, when trying to confirm the accuracy of our predicted liquid–ice VII coexistences using direct coexistence simulations, we observed crystal growth at temperatures significantly above the melting temperature predicted from free-energy calculations. The newly grown parts of the crystal still display the BCC topology of the oxygen atoms, but the crystal shrinks by a few per cent in the direction perpendicular to the growth direction, leading to a slight distortion of the lattice, that we refer to in the following as ice VII*. As this distortion does not occur in fully disordered ice VII, we attribute the unexpectedly high stability of the ice VII* lattice to the emergence of partial proton ordering, which decreases the crystal free energy. To confirm this, we created a fully regrown ice VII* configuration by alternately melting and regrowing the two halves of an ice VII configuration in an elongated simulation box. When measuring the proton–proton and dipole–dipole correlation functions for both the original ice VII structure and the regrown ice VII*, we see only minor changes in the proton–proton correlation function in the region $3 \text{ \AA} < r < 4 \text{ \AA}$ (see Fig-

ure 6(a)). In contrast, the dipole–dipole correlation function (see Figure 6(b)) shows significant additional signal which although weak, extends up to long spatial scales. Using the Frenkel–Ladd method, we calculate the free energy of this configuration (assuming full proton disorder), and find that it is indeed lower than that of the original crystal by $\approx 0.4 \tilde{k}_B T$ per particle, confirming that the lower melting temperature observed in our direct coexistence simulations can be attributed to the (slight) change in crystal structure. The difference in free energy mainly results from the lower potential energy of the regrown crystal. We note here that partial proton ordering would reduce the contribution of the residual entropy to the free energy of the crystal, causing us to underestimate the ice VII* free energy. On the other hand, the presence of defects in the system is expected to cause an overestimate in the crystal free energy. It is thus not a priori obvious that this free energy can be used to predict coexistences. Nonetheless, comparing the melting temperature predicted from the free energy and equations of state of the regrown crystal with the melting temperature taken from the direct coexistence simulations, we find good agreement ($T \approx 320 \text{ K} \pm 5 \text{ K}$ at $P = 250 \text{ MPa}$). Calculating the rest of the coexistence lines for this crystal using thermodynamic integration, we observe that ice VII* has a significantly larger stability region than the original ice VII (see Figure 5).

We note that ices II, III, VI, and 0 are never the most thermodynamically stable phase in the investigated region. For ice III, we checked the stability of both the proton-ordered and fully proton-disordered version, but neither version was

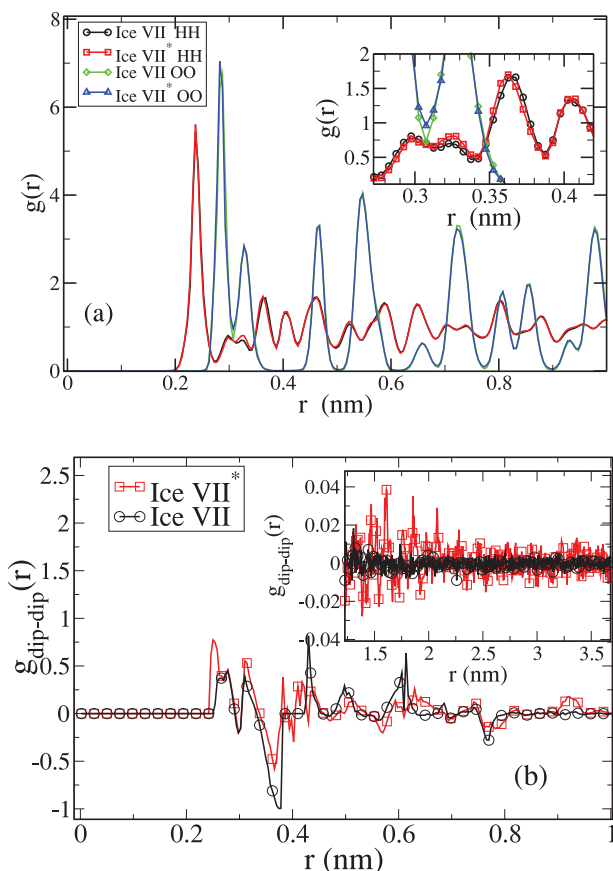


Figure 6. (a) Radial distribution function and (b) dipole–dipole correlation function for the fully proton-disordered ice VII structure and the regrown ice VII* crystal, at $\rho = 1.673 \text{ g/cm}^3$, in the inherent structure. Note the slight extra correlation in $g_{\text{HH}}(r)$ and $g_{\text{dip-dip}}(r)$ in the region $2 \text{ \AA} < r < 4 \text{ \AA}$.

found to be stable with respect to ices I and VII*. In fact, even shifting the free energy of proton-ordered ice III by the full residual entropy associated with full proton disorder does not stabilise the crystal, indicating that a partially ordered ice III (as occurs in real water) would not be stable either. As it may be relevant in future nucleation studies, we include the metastable coexistence line of the liquid with ice 0 in the phase diagram (Figure 5). We note that in the investigated temperature range, ices II and III are more stable than ice 0 only at pressures above approximately 300 MPa.

4. Conclusions

Recently, the ST2 potential has been at the centre of renewed interest in connection to the debate on the origin of the LL critical point [1,45–49]. This model exhibits known deficiencies in accurately modelling water properties, e.g. it overemphasises the tetrahedrality of the liquid structure, thus shifting all water anomalies to higher temperatures. Despite these deficiencies, the ST2 model plays a key role

as a prototype system in many studies related to the presence of an LL critical point. We report here fundamental properties of the ST2 model, by evaluating the location of the gas–liquid critical point and the gas–liquid coexistence curve, as well as the coexistence lines between the liquid and several crystal structures, allowing us to map out the phase diagram of the ST2 model in the low-temperature regime. We find a stable ice I phase at low pressure and temperature, with both the hexagonal and cubic stackings approximately equal in free energy. Differently from real water, the high-pressure phase behaviour of the model is dominated by a new crystal whose growth is templated by the ice VII interface. This ice VII* tetragonal crystal is composed of a lattice in which the oxygens have the same topology as ice VII but in which the protons are not completely randomly distributed. We have not been able to identify a small unit cell for this new crystal, but inspection of the HH radial distribution function indicates minute but observable differences in the region around 3.3 \AA , accompanied by weak but long-ranged correlations in the dipole–dipole correlation function. This structure, despite the small partial proton order, has a significant lower potential energy than VII (approximately 1.2 kJ/mol). As a result, ice VII* is significantly more stable than the fully proton-disordered ice VII phase at all pressures and it dominates the high-pressure phase behaviour of the model. The LL critical point for this model lies, according to the most recent estimates, inside the region of stability of the ice VII* crystal phase and is metastable with respect to ice I_h or I_c as well as to ice VII. Our results provide a starting point for the study of nucleation in the ST2 model, as well as for the exploration of modifications to the model [50] that could make the LL critical point more accessible [18].

Acknowledgements

We thank L. Filion, A. Geiger, A. Rehtanz, and I. Saika-Voivod for useful discussions. Francesco Sciortino acknowledges support from MIUR-PRIN. We are honoured to dedicate this study to Prof. Jean-Pierre Hansen, from whom we have learned liquid-state theory.

Disclosure statement

No potential conflict of interest was reported by the authors.

References

- [1] P.G. Debenedetti and H.E. Stanley, *Phys. Today* **56**, 40 (2003).
- [2] P.H. Poole, F. Sciortino, U. Essmann, and H.E. Stanley, *Nature* **360** (6402), 324–328 (1992).
- [3] F.H. Stillinger and A. Rahman, *J. Chem. Phys.* **60**, 1545 (1974).
- [4] L. Xu, P. Kumar, S.V. Buldyrev, S.H. Chen, P.H. Poole, F. Sciortino, and H.E. Stanley, *Proc. Natl. Acad. Sci. USA* **102** (46), 16558–16562 (2005).

- [5] O. Mishima and H.E. Stanley, *Nature* **396** (6709), 329–335 (1998).
- [6] A.K. Soper and M.A. Ricci, *Phys. Rev. Lett.* **84** (13), 2881–2884 (2000).
- [7] Y. Katayama, T. Mizutani, W. Utsumi, O. Shimomura, M. Yamakata, and K.i. Funakoshi, *Nature* **403** (6766), 170–173 (2000).
- [8] R. Kurita and H. Tanaka, *Science* **306** (5697), 845–848 (2004).
- [9] A. Taschin, P. Bartolini, R. Eramo, R. Righini, and R. Torre, *Nat. Commun.* **4**, 2401 (2013).
- [10] G. Pallares, M.E.M. Azouzi, M.A. González, J.L. Aragones, J.L. Abascal, C. Valeriani, and F. Caupin, *Proc. Natl. Acad. Sci. USA* **111** (22), 7936–7941 (2014).
- [11] K. Amann-Winkel, C. Gainaru, P.H. Handle, M. Seidl, H. Nelson, R. Böhmer, and T. Loerting, *Proc. Natl. Acad. Sci. USA* **110** (44), 17720–17725 (2013).
- [12] M.E.M. Azouzi, C. Ramboz, J.F. Lenain, and F. Caupin, *Nat. Phys.* **9** (1), 38–41 (2013).
- [13] J.A. Sellberg, C. Huang, T.A. McQueen, N.D. Loh, H. Laksmono, D. Schlessinger, R.G. Sierra, D. Nordlund, C.Y. Hampton, D. Starodub, D.P. DePonte, M. Beye, C. Chen, A.V. Martin, A. Barty, K.T. Wikfeldt, T.M. Weiss, C. Caronna, J. Feldkamp, L.B. Skinner, M.M. Seibert, M. Messerschmidt, G.J. Williams, S. Boutet, L.G.M. Pettersson, M.J. Bogan, and A. Nilsson, *Nature* **510** (7505), 381–384 (2014).
- [14] I. Saika-Voivod, F. Sciortino, and P.H. Poole, *Phys. Rev. E* **63**, 011202 (2001).
- [15] V.V. Vasisht, S. Saw, and S. Sastry, *Nat. Phys.* **7**, 549 (2011).
- [16] C.W. Hsu, J. Largo, F. Sciortino, and F.W. Starr, *Proc. Natl. Acad. Sci. USA* **105** (37), 13711–13715 (2008).
- [17] J.L. Abascal and C. Vega, *J. Chem. Phys.* **133** (23), 234502 (2010).
- [18] F. Smallenburg, L. Filion, and F. Sciortino, *Nat. Phys.* **10**, 653 (2014).
- [19] F.W. Starr and F. Sciortino, *Soft Matter* **10** (47), 9413–9422 (2014).
- [20] E. Jagla, *J. Chem. Phys.* **111** (19), 8980–8986 (1999).
- [21] G. Franzese, G. Malescio, A. Skibinsky, S.V. Buldyrev, and H.E. Stanley, *Nature* **409**, 692 (2001).
- [22] L. Xu, S.V. Buldyrev, C.A. Angell, and H.E. Stanley, *Phys. Rev. E* **74**, 031108 (2006).
- [23] P. Gallo and F. Sciortino, *Phys. Rev. Lett.* **109** (17), 177801 (2012).
- [24] D.T. Limmer and D. Chandler, *J. Chem. Phys.* **135** (13), 134503 (2011).
- [25] J.C. Palmer, F. Martelli, Y. Liu, R. Car, A.Z. Panagiotopoulos, and P.G. Debenedetti, *Nature* **510** (7505), 385–388 (2014).
- [26] R.S. Singh and B. Bagchi, *J. Chem. Phys.* **140**, 164503 (2014).
- [27] C.R.C. Buhariwalla, R.K. Bowles, I. Saika-Voivod, F. Sciortino, and P.H. Poole, in press, *Eur. Phys. J. E.* (2015).
- [28] F. Romano, E. Sanz, and F. Sciortino, *J. Chem. Phys.* **134** (17), 174502 (2011).
- [29] A preliminary study of the liquid-ice I_h coexistence line for the ST2 model was carried out by A. Rehtanz, A. Geiger, and P.H. Poole; see A. Rehtanz, Ph. D. thesis, Dortmund University, Logos Verlag, Berlin, 2000.
- [30] D. Frenkel and A.J.C. Ladd, *J. Chem. Phys.* **81** (7), 3188–3193 (1984).
- [31] C. Vega, E. Sanz, J. Abascal, and E. Noya, *J. Phys. Condens. Matter* **20** (15), 153101 (2008).
- [32] J. Russo, F. Romano, and H. Tanaka, *Nat. Mater.* **13** (7), 733–739 (2014).
- [33] D. Quigley, D. Alfè, and B. Slater, *J. Chem. Phys.* **141** (16), 161102 (2014).
- [34] P.H. Poole, S.R. Becker, F. Sciortino, and F.W. Starr, *J. Phys. Chem. B* **115** (48), 14176–14183 (2011).
- [35] E.G. Noya, M.M. Conde, and C. Vega, *J. Chem. Phys.* **129** (10), 104704 (2008).
- [36] B. Smith and D. Frenkel, *Understanding Molecular Simulations* (Academic Press, New York, 1996).
- [37] L. Pauling, *The Nature of the Chemical Bond* (Cornell University Press, Ithaca, 1945), p. 301–304.
- [38] B.A. Berg, C. Muguruma, and Y. Okamoto, *Phys. Rev. B* **75** (9), 092202 (2007).
- [39] P. Virnau and M. Müller, *J. Chem. Phys.* **120** (23), 10925–10930 (2004).
- [40] F. Sciortino, I. Saika-Voivod, and P.H. Poole, *Phys. Chem. Chem. Phys.* **13** (44), 19759–19764 (2011).
- [41] N.B. Wilding, *Phys. Rev. E* **52** (1), 602–611 (1995).
- [42] A.M. Ferrenberg and D. Landau, *Phys. Rev. B* **44** (10), 5081–5091 (1991).
- [43] A. Pelissetto and E. Vicari, *Phys. Rep.* **368** (6), 549–727 (2002).
- [44] M.J. Cuthbertson and P.H. Poole, *Phys. Rev. Lett.* **106**, 115706 (2011).
- [45] G. Franzese, G. Malescio, A. Skibinsky, S.V. Buldyrev, and H. Stanley, *Nature* **409** (6821), 692–695 (2001).
- [46] F. Sciortino, E. La Nave, and P. Tartaglia, *Phys. Rev. Lett.* **91**, 155701 (2003).
- [47] D. Fuentevilla and M. Anisimov, *Phys. Rev. Lett.* **97** (19), 195702 (2006).
- [48] V. Holten, C.E. Bertrand, M.A. Anisimov, and J.V. Sengers, *J. Chem. Phys.* **136** (9), 094507 (2012).
- [49] V. Holten, J.C. Palmer, P.H. Poole, P.G. Debenedetti, and M.A. Anisimov, *J. Chem. Phys.* **140**, 104502 (2014).
- [50] F. Smallenburg and F. Sciortino, submitted (2015).